Grain growth modeling for gas pressure sintering of silicon nitride based ceramics

Thomas Grippi, Stéphanie Béhar-Lafenetre, Holger Friedrich, Daniel Haas, Uwe Schenderlein, Sylvain Marinel, Charles Manière

Grain growth modeling for gas pressure sintering of silicon nitride based ceramics

Thomas Grippi[1,2]*, Stéphanie Béhar-Lafenetre[1], Holger Friedrich[3], Daniel Haas[4], Uwe Schenderlein[4], Sylvain Marinel[2], Charles Manière[2]

1. Thales Alenia Space, 06150, Cannes, France
2. CRISMAT, Normandie Univ, ENSICAEN, UNICAEN, CNRS, 14000, Caen, France
3. Fraunhofer ISC, Center for High Temperature Materials and Design HTL, Bayreuth
4. QSIL Ingenieurkeramic Rauenstein, Germany

Keywords

Silicon nitride, Si_3N_4, Gas pressure sintering, grain growth, model,

1. Abstract

The complexity of liquid phase sintering of silicon nitride implies the use of advanced gas pressure sintering (GPS) industrial process. Sintering additives have been jointly developed to allow the sintering of this challenging material to reach high mechanical properties. The latter properties and GPS process of silicon nitride are strongly influenced by the microstructure development during the thermal treatment under temperature close to 1800°C. In particular, grain growth is a key parameter that needs to be identified. In this work, an experimental design is used to explore microstructural development during the final stage of sintering. The grain size, and porosity data are extracted for different holding times and temperatures to allow the identification of the experimental grain growth. The study is extended to the impact of the heating kinetics regime and the influence of the gas pressure furnace environment.

Graphical abstract

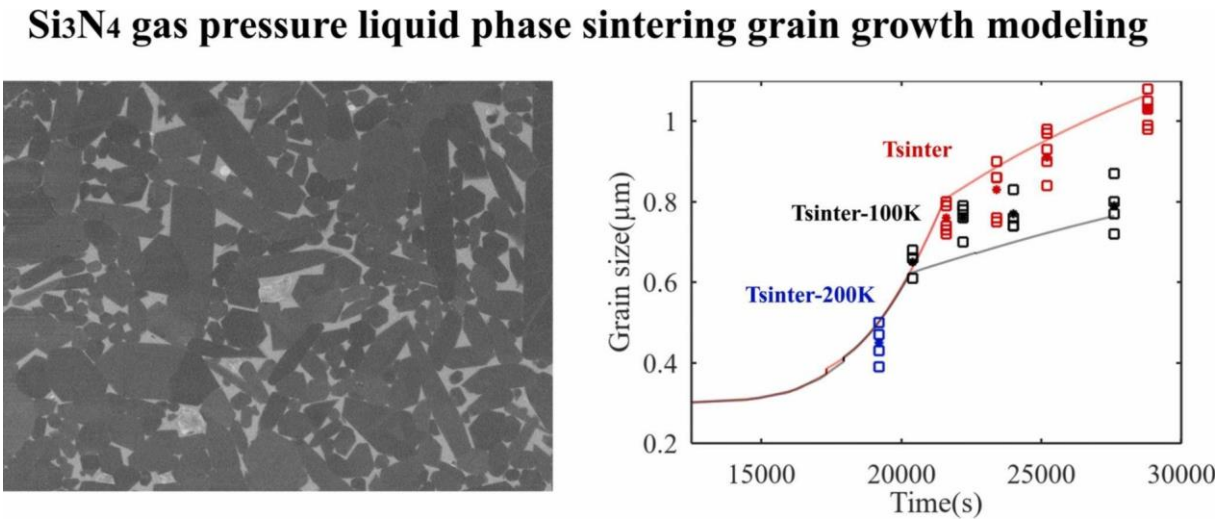

* Corresponding author:
Thomas Grippi, Thales Alenia Space
5Allée des Gabians 06150 CANNES, France
E-mail address: thomas.grippi@thalesaleniaspace.com

Nomenclature

L Linear intercept grain size (m)

X length X of the line on the micrograph (m)

N_L the number of intersections

M Magnification

r Mean particle radius (m)

R Gas constant 8.314 ($J \cdot mol^{-1} \cdot K^{-1}$)

T Temperature (K)

$\dot{G}$ Grain growth rate ($m \cdot s^{-1}$)

G Grain size diameter (m)

G_0 Initial grain size diameter (m)

p Grain growth rate exponent

K Grain growth factor ($m^{1+p} \cdot s^{-1}$)

k_0 Grain growth pre-exponential factor ($m^{1+p} \cdot s^{-1}$)

Q_G Grain growth activation energy ($J \cdot mol^{-1}$)

t Time (s)

t_0 Beginning of holding time (s)

2. Introduction

Si_3N_4 ceramics are widely used in components for optical space applications due to their outstanding mechanical properties and stability in harsh environment. With its high strength, its stiffness and its low coefficient of thermal expansion, silicon nitride is well suited for stable space structures. However, it is extremely difficult to densify Si_3N_4 by pressure-less sintering process, due to the high degree of covalent bonding between nitrogen and silicon, with very low diffusion coefficient of nitrogen or silicon in Si_3N_4. As an example the grain-boundary diffusion of nitrogen is about $D_N \approx 6.37 \times 10^{-24}\ m^2 \cdot s^{-1}$ (at 1400°C) and for silicon about $D_{Si} \approx 3.18 \times 10^{-26}\ m^2 \cdot s^{-1}$ (at 1400°C)[1–4] in Si_3N_4, this is very low compared to the typical value of $D_O \approx 1.37 \times 10^{-20} m^2 \cdot s^{-1}$ (at 1400°C) $D_{Al} \approx 7.11 \times 10^{-23}\ m^2 \cdot s^{-1}$ (at 1400°C) in alumina[5–7]. It is well established that conventional pressure-less sintering methods are hardly applicable to produce pure, dense Si_3N_4 -based ceramics. Most of the sintering processes adapted to silicon nitride to reach dense parts involve the application of pressure: hot pressing[8,9], gas pressure sintering (GPS)[10,11], SPS[12], etc. Among all those sintering methods, the space industry favored the GPS process as it allows sintering of large size parts with complex shapes, since the applied pressure is ensured by a gas. To reach a high density (>98%), liquid phase sintering (LPS) has been developed by using sintering aids. Additives for silicon nitride sintering have been widely explored to date (Y_2O_3, Al_2O_3, MgO, SiO_2, etc.)[13–16]. Fully dense silicon nitride composite based ceramics can now be produced by combining GPS and LPS processes. However, the sintering process applied to large and complex parts for space industry may lead to macroscopic defects such as deformations, cracks, heterogeneous shrinkage, *etc*. Therefore, it is of primary importance to anticipate and minimize the risk of occurrence of these defects. In this context, the modeling of the sintering behavior and FEM simulation of the parts using the continuum mechanic approach are

needed. Consequently, it is mandatory to collect all the physical parameters required to implement a comprehensive model of Si_3N_4 GPS-LPS sintering[17–20]. Among all those input data, there are heat transfer parameters of the whole furnace and sample configuration, the grain growth behavior and the densification kinetics that can be extracted from dilatometric data. This paper is dedicated to the grain growth behavior of Si_3N_4 during the GPS-LPS sintering process. The latter is a key aspect in the understanding of the final stage sintering microstructural development. In addition grain growth may influence the diffusion path motion in the liquid phase and the final part mechanical resistance. The grain growth is a consequence of the dissolution-precipitation mechanism (Ostwald ripening)[21] and can be influenced by the nature of the liquid phase composition[22]. In this article, the grain growth behavior is identified based on isothermal tests [3] and analytic modeling.

3. Experimental

3.1. Thermal cycle

The furnace used is located at the Fraunhofer ISC, Center for High Temperature Materials and Design HTL, Bayreuth [23]. This device is a vertically oriented cylindrical furnace. The heating is provided by graphite tubes located radially inside the furnace. The furnace's wall, its top and base sections are both water-cooled. The studied material is a grade of silicon nitride provided by QSIL. Two debinded cylinders ø10x10mm samples are sintered for each cycle. Each sample is in a different configuration:

- **Configuration 1** refers to the *"window configuration"*, which is used for optical dilatometry. In this configuration the sample is located inside two crucibles with two holes each in opposite positions for sample observation (see Figure 1).
- **Configuration 2** refers to the "*closed crucible configuration*", a smaller closed crucible, in which a sample is located, as a witness sample for comparison. This sample configuration is more stable and less sensitive to the atmosphere and gas flow/convection that could differ from one cycle to another (see Figure 1).

In both configurations, the sample is surrounded by scrap material (Si_3N_4 crushed elements made of the same composition as the samples) that reproduces the conditions of sintering in an industrial furnace.

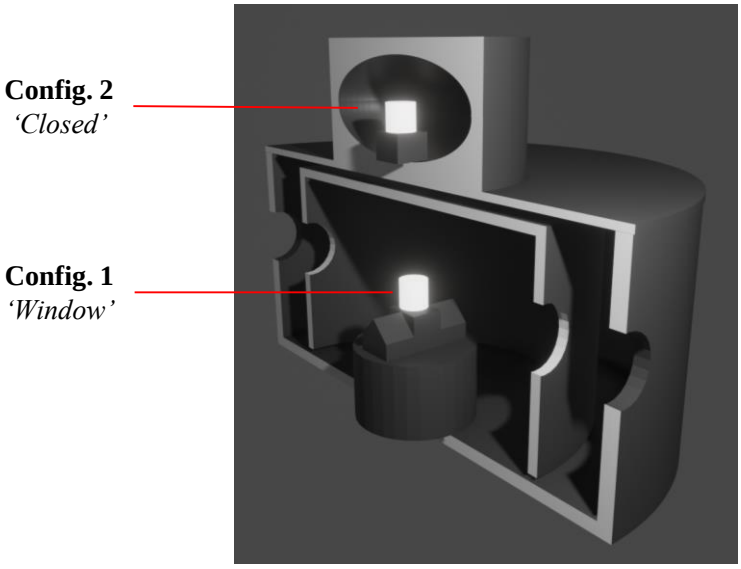

Figure 1 Cross section of the sintering configuration

The objective of this study is to conduct the microstructure analysis during the intermediate and final stage of densification (grain growth, pore size and coalescence, density, etc.). To conduct this study, 8 isothermal interrupted tests are planned: 4 at Tsinter – 100 K and 4 at Tsinter, with a 5 K/min high temperature heating rate, Tsinter being a common temperature reached during the sintering process, close to 1800°C (Figure 2). A last test is planned at Tsinter – 200 K without dwelling in order to have 3 different temperatures during the heating ramp (anisothermal behavior study case). For all experiments, the thermal cycles were run and the heating was switched off when the different temperature-time points were achieved. The aim is to reveal the interrupted cycle microstructure. This study is made by taking a representative industrial sintering cycle as a reference. Interruptions of the cycles at different times are conducted (full holding time, 0.5*holding time, 0.25*holding time and 0 min holding time) by maintaining the same sintering conditions: gas pressure, heating ramp, samples configuration (see Figure 2).

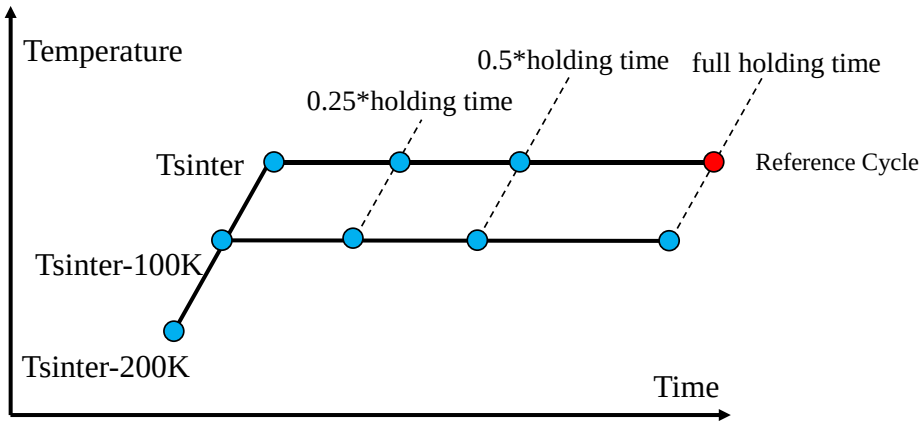

Figure 2 Schematic of interrupted cycles study, Tsinter~1800°C

3.2. Data collecting and grain size determination

The microscope used was JEOL JSM 7200F equipped with a Robinson-type back scattered electron diffusion detector (BED-C). Each sample was cut at half height and mirror polished. A micrograph at magnification x500 and at least 6 pictures between the center and the border at magnification x10.000 were taken as shown in Figure 3.

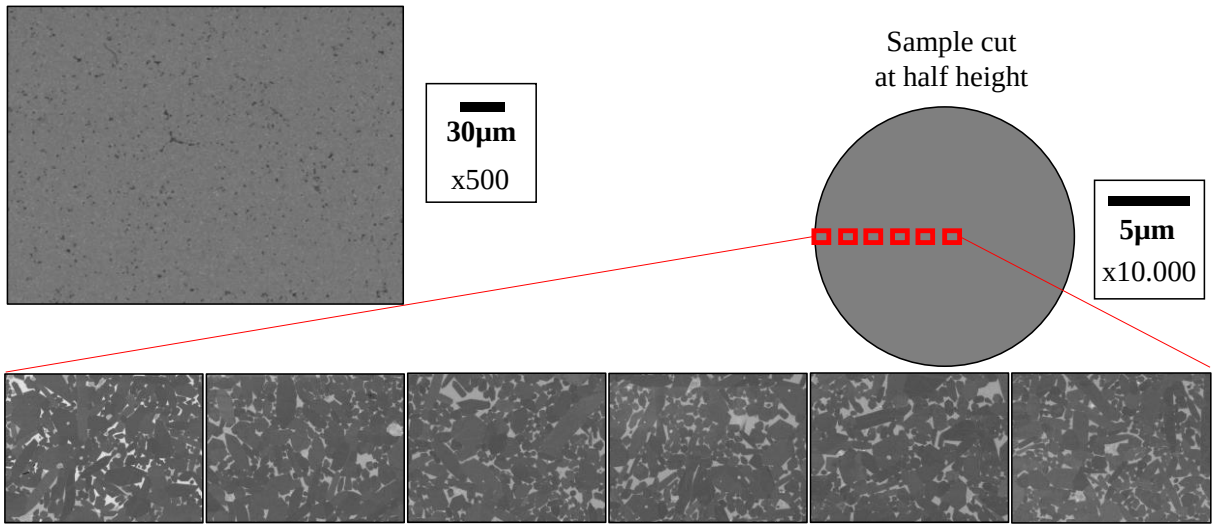

Figure 3 Schematic view of the range of SEM micrographs taken for each sample.

The first step of the grain growth measurement consists in a linear intercept. This step is done manually, the user of this method counts the grain borders and calculates the mean grain size with a stereological factor[24,25].

$$L = \frac{X}{MN_L} \quad (1)$$

By knowing the length X of the line on the micrograph (for instance the border of the microstructure picture on the left Figure 4), M the magnification and NL the number of intersections, the mean intercept length L can be determined. To take into account the multi-phase microstructure (amorphous phase, porosity, …), the ratios of these phases were estimated for each image (see right picture in Figure 4) As it is recommended by the work of Wurst and Nelson [26], the expression of N_L is replaced by $N_L = N_{ss} + N_{sv}/2$, where N_{ss} refers to a solid-solid boundary and N_{sv} refers to a solid-vapor boundaries (the porosity and in our case, also the amorphous phase is counted as thick grain boundary). Concerning the value of X in presence of porosity and liquid phase, the effective value of X is corrected by multiplying this term by the Si_3N_4 granular phase ratio [26].

Based on multiple-linear intercepts and the different SEM images, a mean intercept (L) value can be calculated. The mean grain size is calculated *via* a stereological factor from a 1-dimension value to 3-dimensions[27]:

$$G = 1.56\bar{L} \quad (2)$$

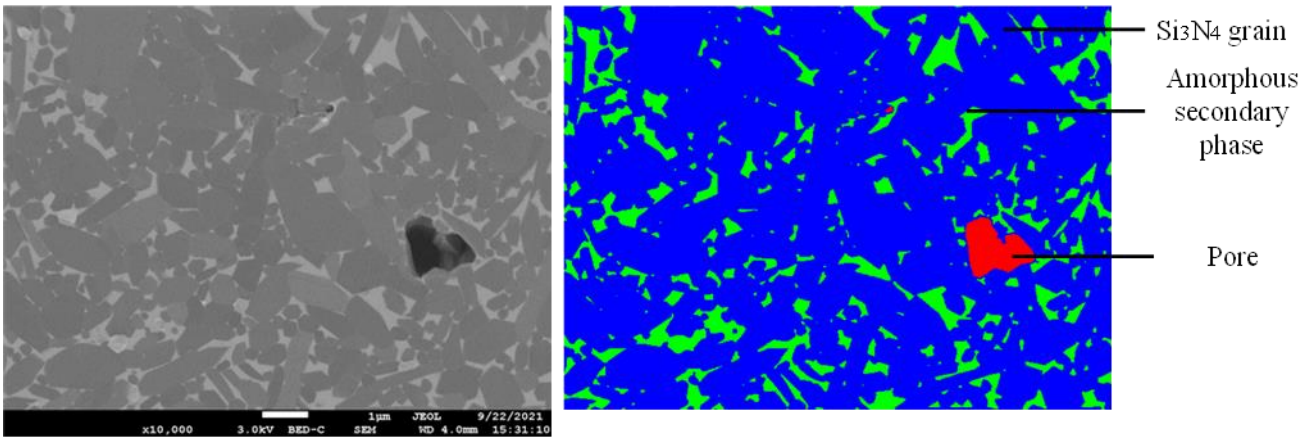

Figure 4 (Left) linear intercept on a Si_3N_4 polished surface sample micrograph at x10.000. (Right) colored micrograph for the calculation of phase proportions (Si_3N_4 grains in blue, the amorphous secondary phase in green and pores in red)

The Figure 4 shows the SEM microstructures of samples previously mirror-polished. The typical Si3N4-based ceramic microstructure is observed: Si3N4 grains and amorphous secondary phase (coming from the liquid phase at high-temperature).

3.3. Grain growth model identification method

In order to determine the grain growth behavior during all the industrial thermal cycle, the linear intercept method (Figure 2) will be employed to determine the average grain size of each test. The collected data will be fitted mathematically for the two temperatures to determine the experimental grain growth kinetics. The isothermal grain growth behavior will be identified and modeled with GNU Octave, for verification. As the grain growth shows a slightly different regime in the ramping stage, a second anisothermal identification will be conducted to correct the first behavior to be identified (isothermal behavior). Finally, the grain size prediction in the whole thermal cycle will be compared to the experimental data for a final check.

4. Results and discussion

4.1. SEM characterizations

The grain growth can be seen as a function of temporal interruptions on SEM micrographs at x10,000 in Figure 5. The density evolution during the temperature holding has also been compared as a function of holding at “Tsinter” in red and “Tsinter-100K” in black, as can be observed on micrographs at x500. The apparent relative density stagnates in the case of the isotherm at “Tsinter-100K”, at 89% of relative density. For the isotherm at “Tsinter”, 99.7% of relative density is reached by the end of the cycle.

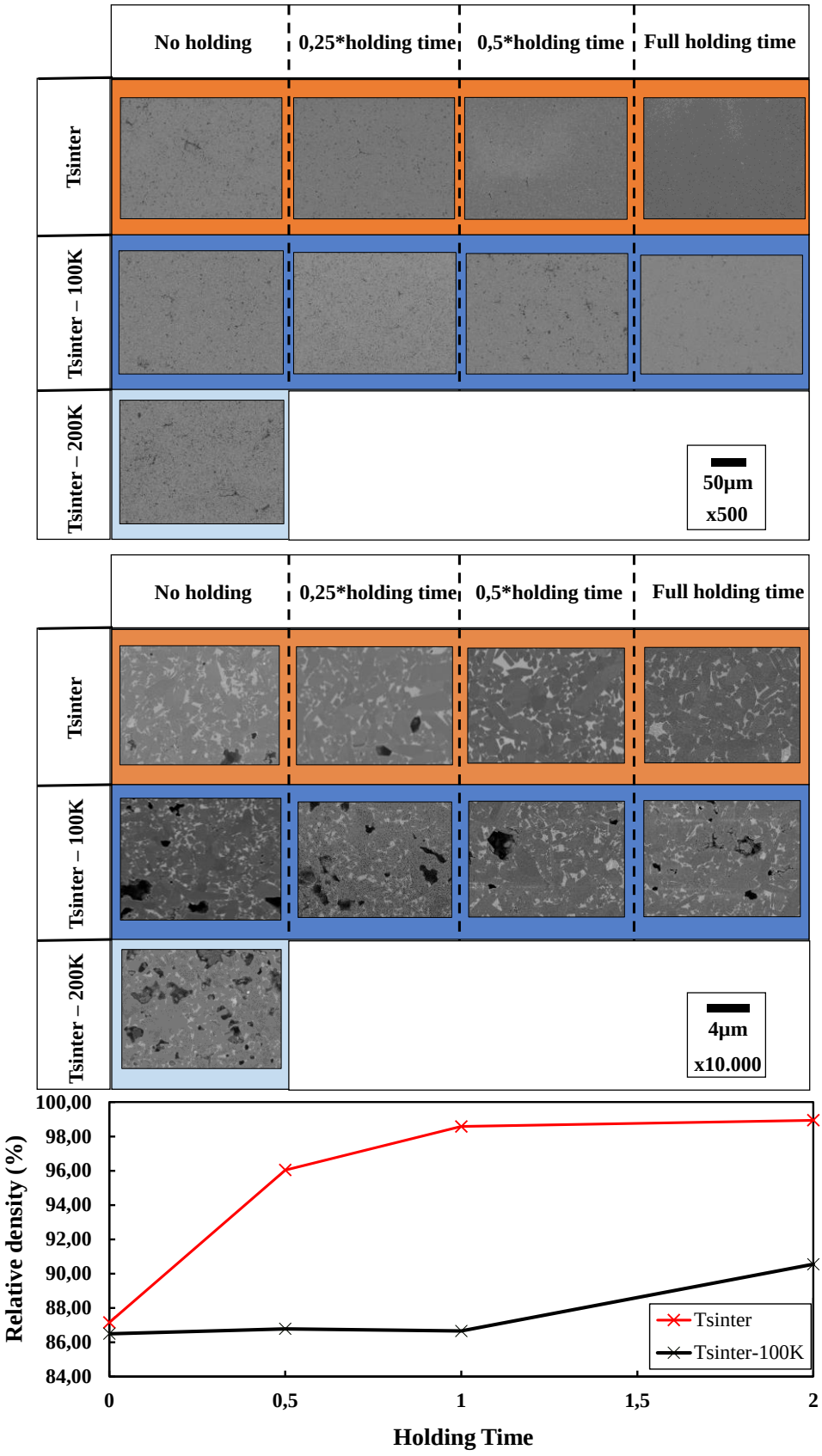

Figure 5 SEM micrographs for each quench, at magnification x500 (top), at magnifying x10.000 (middle) and corresponding relative density(bottom graph).

Each picture gives a mean grain size (with linear intercept method[24–26]). For each cycle, the analysis has resulted into a cloud of data reported in Figure 6. As a first check, it is interesting to compare both configurations (configurations 1 and 2) with the values of isotherms at Tsinter. As can be seen, for both configurations the grain size varies from a mean value of 0.75 µm to 1.00 µm at the end of the cycle (Figure 6). The difference is negligible and shows that there is no drastic microstructure difference between both configurations. As the 2 configurations are very similar, the presented study focuses on data from the configuration 1 (crucible with the window). Indeed, this resulting grain growth model will be implemented with the final sintering model that will be based on the sample in this same configuration i.e. in the "window" crucible, to be studied in-situ (TOM dilatometry configuration).

From the method of analysis, it has been observed that data extracted from micrographs captured in zones closer to samples' borders, lead to larger grain values (see in Figure 6). These larger mean diameters, near the surface, may be explained by pollution elements, vapor transports[3,22] but not temperature gradients as it is distributed like a thin skin. As the granular growth study is focusing on the core behavior and not precisely on surface aspects, these values have been taken out from the data processing.

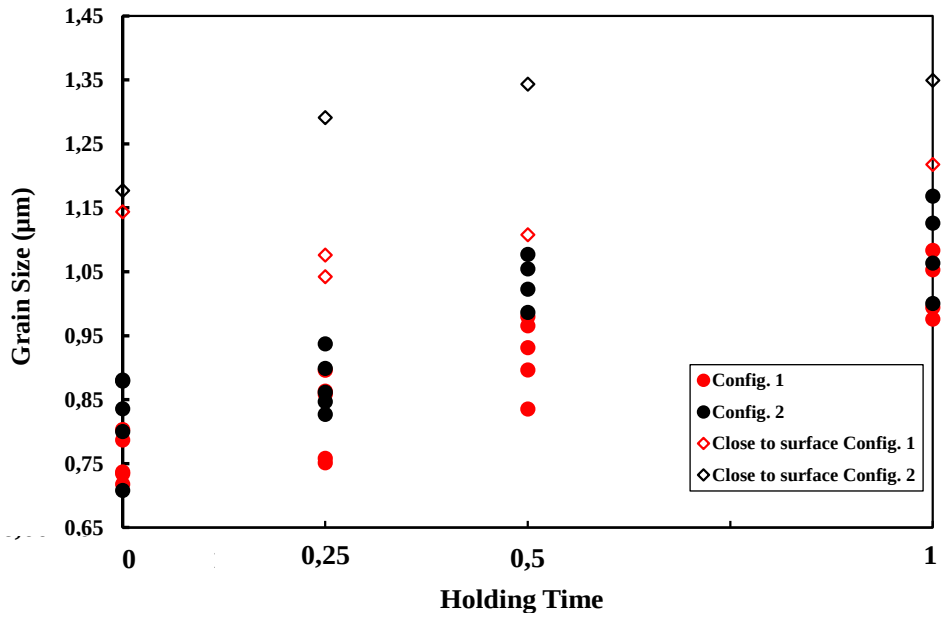

Figure 6 Grain growth as a function of holding time for 2 configurations at Tsinter

4.2. Isothermal grain growth identification

As described in the previous part, each sample has been analyzed and a grain size has been determined for each cycle, based on SEM pictures. The grain size versus time and temperature can now be computed. From grain size values, the evolution of G has been fitted mathematically. The grain growth fitting function uses the following formula:

$$G_{fit} = A \times t^{B} + C \quad (3)$$

where *t* is a time variable and A, B and C are fitting constants.

The fitted expressions and experimental data points are reported in Figure 7.

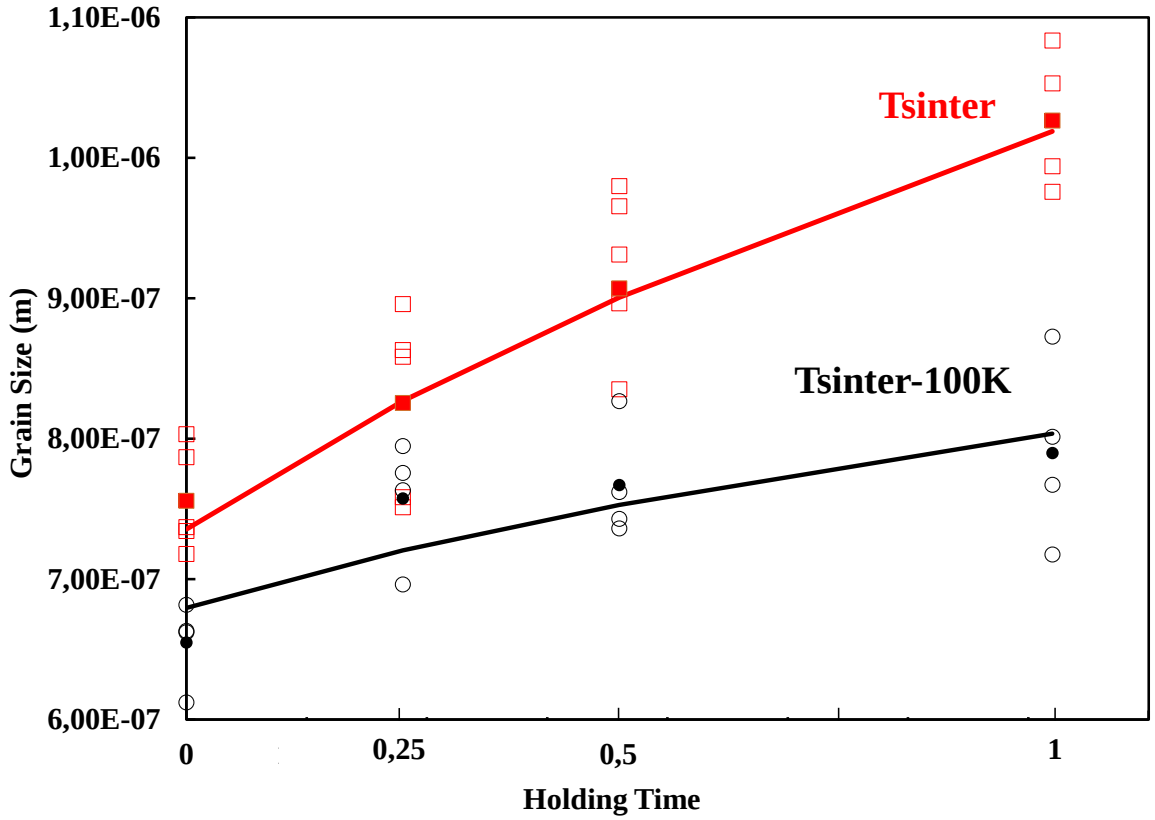

Figure 7 Mathematical fit for 2 different temperatures and grain size as a function of holding time

From this G_{fit} function, the grain growth rate ($\dot{G}_{fit}$) has been determined.

In liquid phase sintering, the grain growth may come from a dissolution-precipitation mechanism (Ostwald ripening) and obeys similar grain growth kinetics than in the solid-state case[3].

$$\dot{G} = \frac{K(T)}{G^p} \; with \; K(T) = k_0 \exp\left(-\frac{Q_G}{RT}\right) \quad (4)$$

If the rate controlling grain growth mechanism is the diffusion through the liquid phase, the exponent (*p)* equals 2. This exponent's value equals 1 for interface reaction mechanisms.

In order to determine experimentally the grain growth mechanism from the experimental grain growth kinetic data, the previous rate equation is linearized.

$$\ln\left(\dot{G}\right) = \ln(K(T)) - p \times \ln(G) \quad (5)$$

The linear regression is reported in Figure 8 a., for each temperature. From these curves, a mean value of p=1.93 is obtained indicating a dominant grain growth mechanism of diffusion through the liquid phase. From each temperature intercept in Figure 8 a. the corresponding K(T) value can be determined. By using a second linear regression below, the isothermal regime values of k_0 and Q_G can be determined (see Figure 8 b.).

$$\ln(K(T)) = \ln(k_0) - \frac{Q_G}{RT} \quad (6)$$

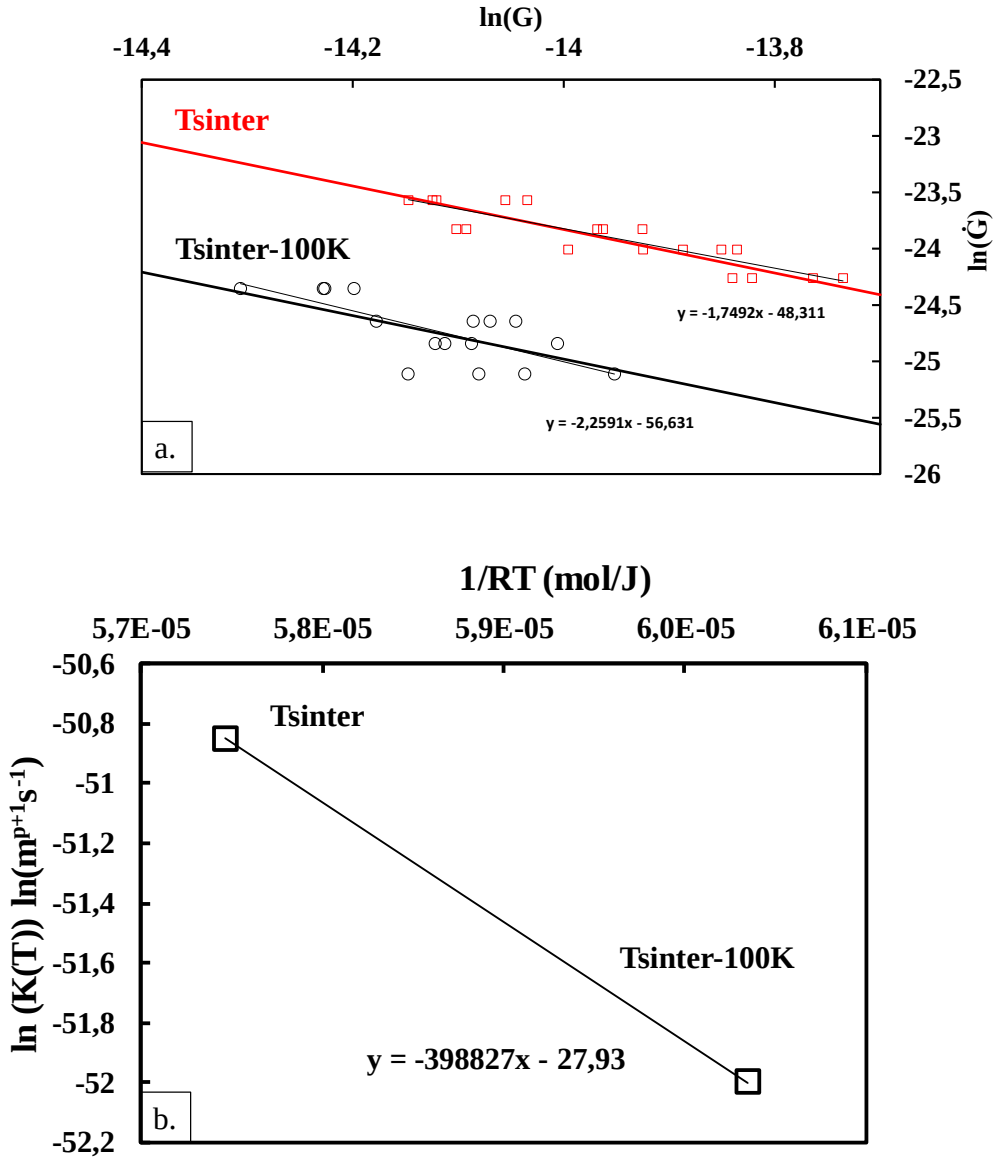

Figure 8 (a.) Linearization and identification of the parameter p, (b.) Linearization and identification of Q_G and k_0

Based on Figure 8 b., Q_G and k_0 values of 399kJ/mol and k_0= 7,41575E-13 $m^{1+p} \cdot s^{-1}$ have been obtained respectively.

This first couple of parameters has been determined using the data from the isothermal conditions. As can be inferred from the Figure 9 below, the parameters are reliable in the case of the isothermal conditions, on the model computed analytically.

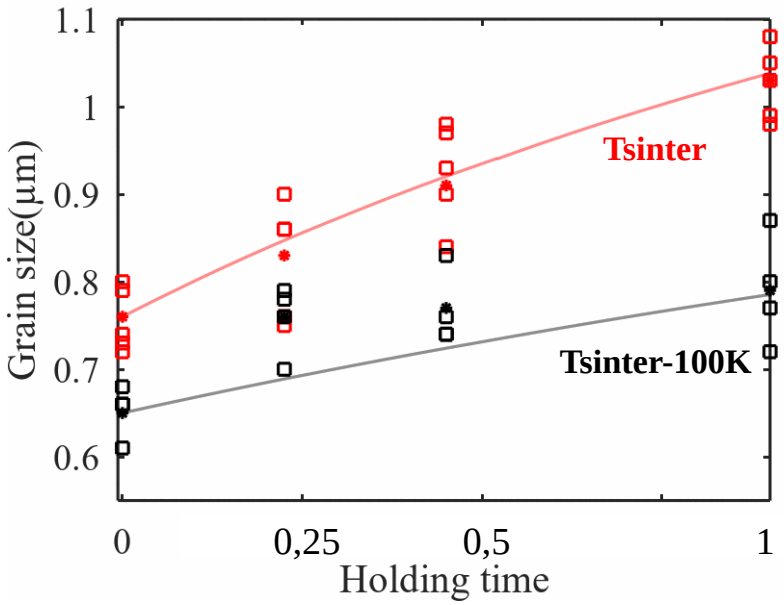

Figure 9 Modeling of grain growth for 2 different temperatures holding on Octave

In a second investigation, the same parameters have been used to compute the full cycle shown below on Figure 10. In this particular case, the parameters identified should be able to fit the heating part experimental data and then the holding part data. However, as shown in Figure 10, these parameters have failed to reproduce the whole cycle starting from a 0.27 µm mean grain size (measured after debinding process). It can be deduced that different grain growth kinetics lead to this apparent gap between the grain growth rate in anisothermal and isothermal cases. In Figure 5, a high proportion of small grains are present in the beginning. These grains have a high solubility (Ostwald ripening) and may be a possible explanation for these two grain growth regimes. Faster grain growth rate may be required in the heating part. A phase transition from initial α grains to β phase may also explain such regime change of grain growth during the heating.

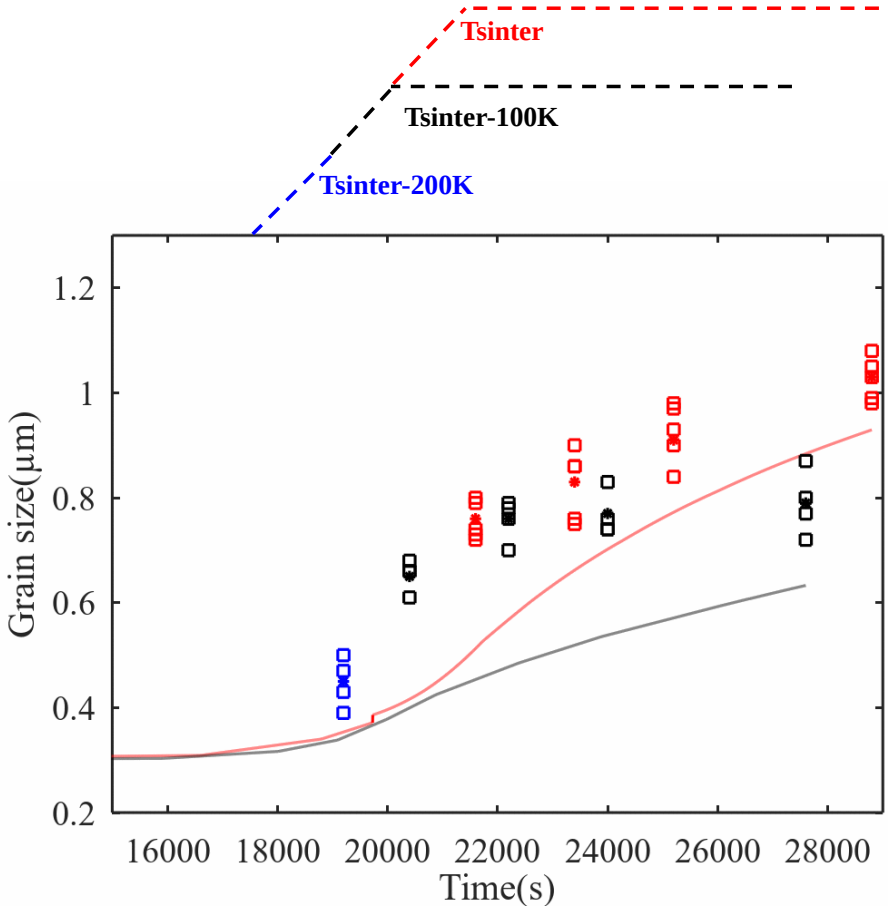

Figure 10 Isothermal grain growth behavior applied to the whole sintering cycle.

4.3. Anisothermal (ramping) stage grain growth identification

In order to model the whole cycle grain growth, the behavior is split into two behaviors :

-**Anisothermal** grain growth behavior during the heating part of the cycle.

-**Isothermal** grain growth behavior during the holding temperature.

To identify the anisothermal grain growth regime, the experimental data collected between "Tsinter-200K", "Tsinter-100K" and "Tsinter" will be employed. The analysis is processed in a similar way to the first part described above. The grain growth mechanism parameter (p) identified in isothermal regime is assumed to be the same as in the anisothermal case. The parameter required to be adapted to this case is the activation energy Q_G and the pre-exponential factor k_0. To do so, grain size data (0min holding times points) have been fitted

for each temperature with the following function that corresponds to the grain growth behavior in ramping stages:

$$G_{fit} = A \times e^{Bt} \quad (7)$$

where t is a time variable in second, A and B are constants. The anisotherm fitting is reported in Figure 11.

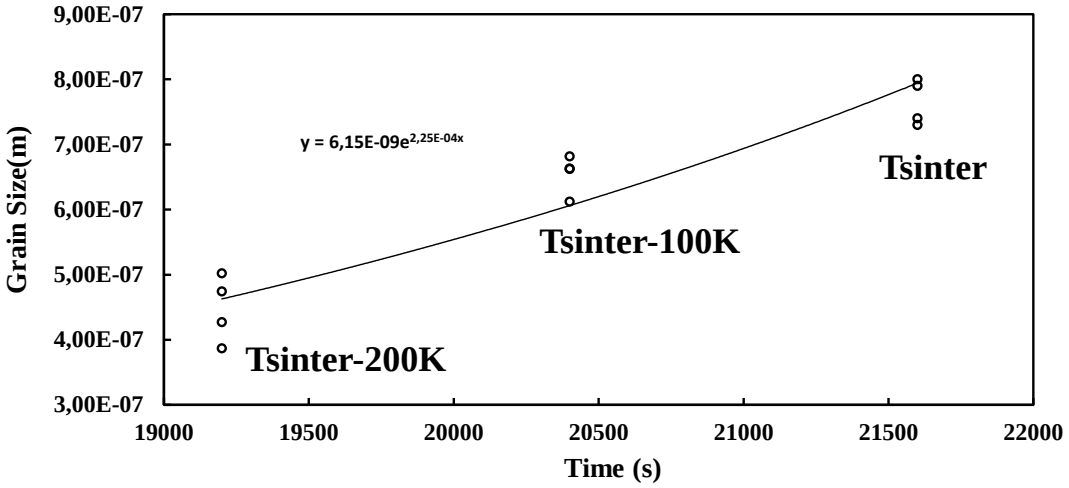

Figure 11 Mathematical fit for grain growth during the heating part (5K/min heating rate)

From this fitting, the grain growth rate $\dot{G}$ has been expressed. Assuming the same mechanism (p parameter identified before), it is possible to calculate the anisotherm $K(t)$ formula:

$$K(t) = G^p \dot{G} \quad (8)$$

Using the following anisotherm linearization, k_0 and Q_G can be determined.

$$\ln(G^p \dot{G}) = \frac{Q_G}{RT} + \ln(k_0) \quad (9)$$

From the linearization in Figure 12, we obtain for the anisotherm regime: Q_G=262kJ/mol and k_0=1,009E-15 $m^{1+p} \cdot s^{-1}$.

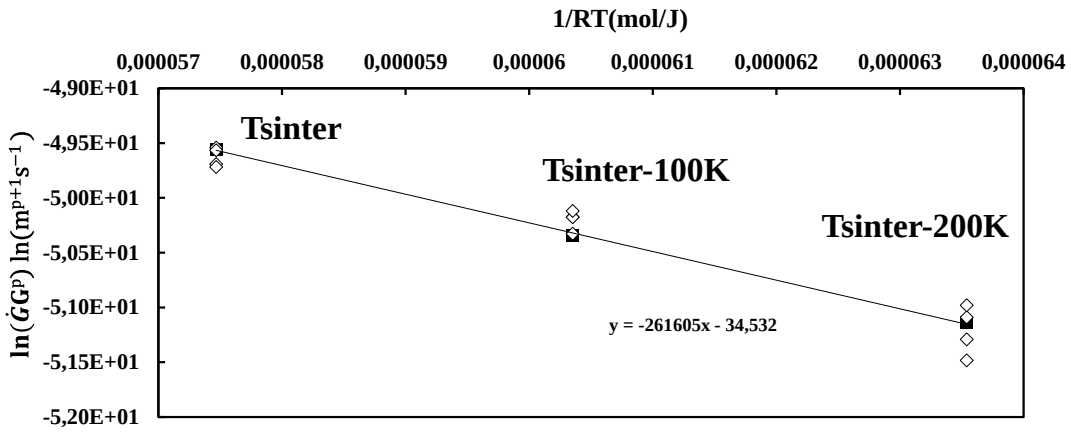

Figure 12 Linear regression to identify Grain growth activation energy during the heating

Now all the parameters identified are adapted to the anisothermal case, and the modeling can be done for verification. In this precise case, only the heating part is studied to check that extracted parameters are able to model and fit the grain size experimental data. As shown below on Figure 13, this couple of parameters are more adapted to this ramping case for both temperatures. The following step focuses on the combination of these parameters couples.

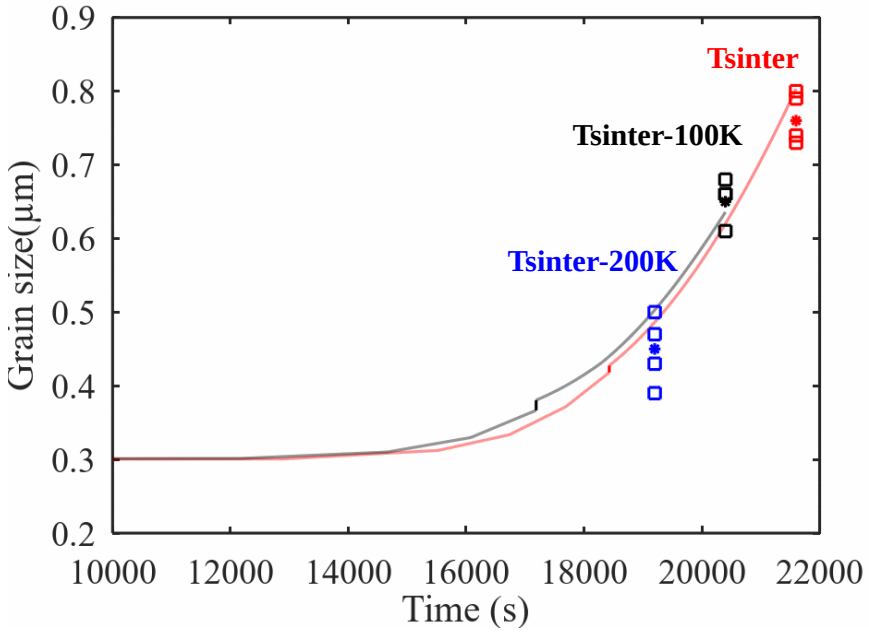

Figure 13 Grain growth model with a new range of parameters adapted to heating part.

4.4. General grain growth model verification

In this part, as the two models are fitting for their own part, the combination of both approaches must be carried out to have the most comprehensive model for each temperature rate, anisothermal and isothermal stages. The two models have been combined with a sigmoidal function (f_0) that switches parameters identified in isothermal (case 1) to parameters identified in ramping (case 2). In the present case, this sigmoid has done a switch for the parameters Q_G and k_0: from Q_{G1} and k_{01} for case 1 to Q_{G2} and k_{02} for case 2 at the right time.

$$\begin{cases} f_0 = \frac{1}{1+e^{-(t-t_0)}} \\ Q_G = Q_{G1}(1-f_0) + Q_{G2}(f_0) \\ k_0 = k_{01}(1-f_0) + k_{02}(f_0) \end{cases} \quad (10)$$

The experimental grain growth is well fitted by these combined grain growth models (see Figure 14). This whole model is now fully comprehensive of the cycle variations.

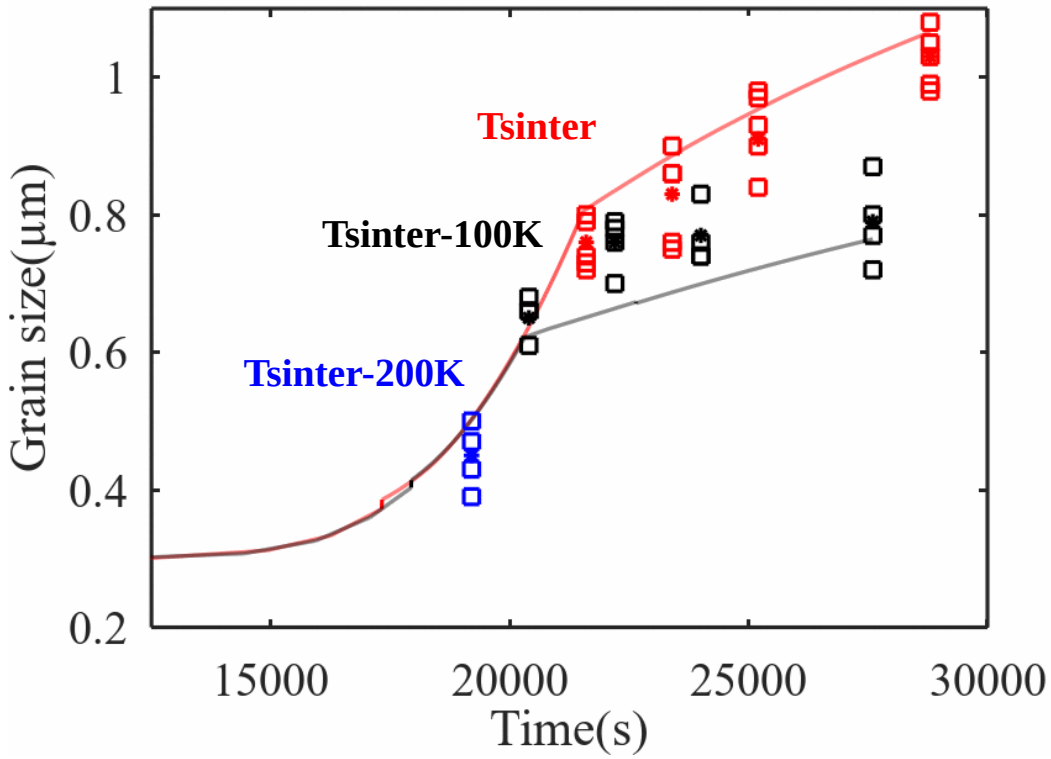

Figure 14 Full grain growth fitting anisothermal case and isothermal case

5. Conclusion

Based on micrographs of quenches on an industrial sintering cycle, it was possible to extract the microstructural development behavior of Si_3N_4 during a gas pressure sintering. This liquid phase sintering process exhibits a grain growth behavior by diffusion through the liquid phase with a grain size exponent of p=2. The grain growth model points out a complex behavior with higher grain growth kinetics in the beginning of the cycle during the heating. This dissimilar grain growth behavior is possibly explained by the high proportion of small grains that easily dissolves in the initial microstructure or to phase transition. With a step like function, a comprehensive model allows reproducing the grain growth experimental data for the whole industrial cycle. This grain growth model will be coupled to a densification model for a comprehensive simulation of silicon nitride sintering

6. Acknowledgement

The author thanks Christelle Bilot for her help in the SEM images of this study. We would like to thank Thales Alenia Space for the PhD subvention of the author (CIFRE Thesis Contract CIFRE N° 2019/1366). A collaboration between four entities has been needed, FCTI (industry) has provided the debinded specimens, the advanced gas sintering equipment of the Fraunhofer HTL has been used for the experimental sintering test, the modeling/simulation study is processed at the CRISMAT laboratory, and the assessment of the results for space applications is done by Thales Alenia Space.

7. Credit authorship contribution statement

Thomas Grippi: Conceptualization, Supervision, Experimentation, Modeling, Writing; **Stephanie Behar-Lafenetre:** Conceptualization, Supervision, Review & Editing; **Daniel Haas:** Experimentation, Review & Editing; **Uwe Schenderlein**: Experimentation, Review & Editing **Holger Friedrich:** Conceptualization, Experimentation, Supervision, Review &

Editing; **Sylvain Marinel:** Supervision, Conceptualization, Review & Editing. **Charles Maniere:** Supervision, Conceptualization, Modeling, Writing, Review & Editing

8. References

[1] G. Petzow, M. Herrmann, Silicon Nitride Ceramics, Structure and Bonding. (2002) 47–167. https://doi.org/10.1007/3-540-45623-6_2.

[2] R.M. German, Sintering Theory and Practice, Wiley, Wiley, 1996. http://www.wiley.com/WileyCDA/WileyTitle/productCd-047105786X.html.

[3] M.N. Rahaman, Sintering of Ceramics, CRC Press, 2007.

[4] D. Bernache-Assollant, Frittage : aspects physico-chimiques Partie 2 : frittage en phase liquide, Techniques de l'Ingénieur 33, 1–12, 2014.

[5] Y. Oishi, W.D. Kingery, Self-Diffusion of Oxygen in Single Crystal and Polycrystalline Aluminum Oxide, The Journal of Chemical Physics. 33 (1960) 480–486. https://doi.org/10.1063/1.1731170

[6] R.H. Doremus, Diffusion in alumina, Journal of Applied Physics. 100 (2006) 101301. https://doi.org/10.1063/1.2393012.

[7] S. Matsubara, K. Tarada, T. Kobayashi, T. Saitou, M. Umeda, Y. Mihara, K. Oide, H. Shin, Y. Katsuda, A set of constitutive functions for dried body to predict entire deformation process of ceramic products during firing, EC. 34 (2017) 2668–2697. https://doi.org/10.1108/ec-12-2016-0444.

[8] L.J. Bowen, R.J. Weston, T.G. Carruthers, R.J. Brook, Hot-pressing and the phase transformation in silicon nitride, J. Mater. Sci. 13 (1978) 341–350 https://doi.org/10.1007/BF00647779.

[9] L.J. Bowen, T.G. Carruthers, R.J. Brook, Hot-Pressing of Si_3N_4 with Y_2O_3 and Li_2O as Additives, Journal of the American Ceramic Society. 61 (1978) 335–359. https://doi.org/10.1111/j.1151-2916.1978.tb09323.x.

[10] M. Mitomo, N. Yang, Y. Kishi, Y. Bando, Influence of powder characteristics on gas pressure sintering of Si_3N_4, J. Mater. Sci. 23 (1988) 3413–3419. https://doi.org/10.1007/BF00551328.

[11] M. Mitomo, Pressure sintering of Si_3N_4, J Mater Sci. 11 (1976) 1103–1107. https://doi.org/10.1007/BF02396645.

[12] O.A. Lukianova, V.Y. Novikov, A.A. Parkhomenko, V. V. Sirota, V. V. Krasilnikov, Microstructure of Spark Plasma-Sintered Silicon Nitride Ceramics, Nanoscale Res Lett. 12 (2017) 0–5. https://doi.org/10.1186/s11671-017-2067-z.

[13] F.L. Riley, Silicon Nitride and Related Materials, Journal of the American Ceramic Society. 83 (2004) 245–265. https://doi.org/10.1111/j.1151-2916.2000.tb01182.x.

[14] Z. Huang, L. Wu, Phase Equilibria Diagrams of High Temperature Non-oxide Ceramics, Springer Singapore, 2018. https://doi.org/10.1007/978-981-13-0463-7.

[15] F.F. Lange, S.C. Singhal, R.C. Kuznicki, Phase Relations and Stability Studies in the Si_3N_4-SiO_2-Y_2O_3 Pseudoternary System, Journal of the American Ceramic Society. 60 (1977) 249–252. https://doi.org/10.1111/j.1151-2916.1977.tb14118.x.

[16] V.V. Krasil'nikov, V.V. Sirota, A.S. Ivanov, L.N. Kozlova, O.A. Luk'yanova, V.V. Ivanisenko, Investigation of the Structure of Si3N4-Based Ceramic with Al2O3 and Y2O3 Additives, Glass Ceram. 71 (2014) 15–17. https://doi.org/10.1007/s10717-014-9606-1.

[17] S.J. Park, P. Suri, E. Olevsky, R.M. German, Master sintering curve formulated from constitutive models, Journal of the American Ceramic Society. 92 (2009) 1410–1413. https://doi.org/10.1111/j.1551-2916.2009.02983.x.

[18] R. Bollina, S.J. Park, R.M. German, Master sintering curve concepts applied to full-density supersolidus liquid phase sintering of 316L stainless steel powder, Powder Metallurgy. 53 (2010) 20–26. https://doi.org/10.1179/174329009X409688.

[19] J. Wang, R. Raj, Estimate of the Activation Energies for Boundary Diffusion from Rate-Controlled Sintering of Pure Alumina, and Alumina Doped with Zirconia or Titania, Journal of the American Ceramic Society. 73 (1990) 1172–1175. https://doi.org/10.1111/j.1151-2916.1990.tb05175.x.

[20] F. Raether, P. Schulze Horn, Investigation of sintering mechanisms of alumina using kinetic field and master sintering diagrams, Journal of the European Ceramic Society. 29 (2009) 2225–2234. https://doi.org/10.1016/j.jeurceramsoc.2009.01.025.

[21] L. Sun, C.-C. Jia, M. Xian, A research on the grain growth of WC–Co cemented carbide, International Journal of Refractory Metals and Hard Materials. 25 (2007) 121–124. https://doi.org/10.1016/j.ijrmhm.2006.03.002.

[22] M. Hotta, J. Hojo, Inhibition of grain growth in liquid-phase sintered SiC ceramics by AlN additive and spark plasma sintering, Journal of the European Ceramic Society. 30 (2010) 2117–2122. https://doi.org/10.1016/j.jeurceramsoc.2010.04.006.

[23] F. Raether, R. Springer, S. Beyer, Optical dilatometry for the control of microstructure development during sintering, Materials Research Innovations. 4 (2001) 245–250. https://doi.org/10.1007/s100190000101.

[24] E.E. Underwood, Quantitative Stereology for Microstructural Analysis, Microstructural Analysis. (1973) 35–66. https://doi.org/10.1007/978-1-4615-8693-7_3.

[25] A.P. Tomsia, A.M. Glaeser, eds., Ceramic Microstructures, Springer US, 1998. https://doi.org/10.1007/978-1-4615-5393-9.

[26] J.C. Wurst, J.A. Nelson, Lineal Intercept Technique for Measuring Grain Size in Two-Phase Polycrystalline Ceramics, J. American Ceramic Society. 55 (1972) 55–109. https://doi.org/10.1111/j.1151-2916.1972.tb11224.x.

[27] M.I. Mendelson, Average Grain Size in Polycrystalline Ceramics, J American Ceramic Society. 52 (1969) 443–446. https://doi.org/10.1111/j.1151-2916.1969.tb11975.x.

Figure captions